Eur. J. Mech. B/Fluids 18 (1999) 847–867

Wall shear stress and void fraction in Poiseuille bubbly flows: Part II: experiments and validity of analytical predictions

N. Rivière [a], A. Cartellier [a,*], L. Timkin [b], O. Kashinsky [b]

[a] *Laboratoire des Écoulements Géophysiques et Industriels (INPG-CNRS-UJF), BP 53, 38041 Grenoble cedex, France*
[b] *Institute of Thermophysics, 630090 Novosibirsk, Russia*

(Received 27 April 1998; accepted 24 April 1999)

Abstract – In a companion paper, a simple analytical formulation has been established which provides the wall shear stress in laminar bubbly flows for idealised transverse void fraction distributions. In the present paper, this approach is applied to Poiseuille bubbly flows in circular ducts. New measurements of the void fraction profiles and wall friction angular distribution in a pipe are presented for a wide range of flow parameters. Approximating the void profiles by step-functions allows us to evaluate the wall friction with the above mentioned model. Results are shown to agree satisfactorily with measurements. Notably, negative wall shear stress and wall shear stress much higher than their single-phase flow counterpart at the same liquid flow rate are recovered. Therefore, the principal mechanisms responsible for friction modification are captured with this simple model.

dispersed flows / Poiseuille bubbly flow / wall shear stress / void fraction distribution / two-fluids model

1. Introduction

In a previous paper (Rivière and Cartellier [1]), it was shown that, for a sub-class of laminar bubbly flows, the wall shear stress can be connected to the structure of the void fraction transverse distribution by simple analytical formula. The behaviour predicted by this model was found to agree qualitatively with experimentally observed trends. Indeed, two important aspects were recovered, namely, the appearance of secondary flows and the fact that the wall shear stress in two-phase conditions can be larger than the wall shear stress in one phase conditions at the same liquid flow rate. Quantitative agreement has also been obtained for plane Poiseuille bubbly flows, but the set of data available was limited.

In order to better appreciate the range of validity of the model, it has been decided to check it against the data base already available at the Institute of Thermophysics for Poiseuille bubbly flows in a cylindrical duct. To strengthen the comparison, additional experiments have been performed in the same pipe for a higher liquid viscosity.

The paper is organised as follows. First, following closely the developments presented in [1], the analytical formula connecting the wall shear stress to the void profile is derived for a cylindrical duct (section 2). Then, after a brief description of the experimental set-up and the measuring techniques (section 3.1), a new set of void fraction profiles and of wall shear stress data are presented (section 3.2). In section 4, predicted and measured values of the wall shear stress are compared, and the limits of validity of the analytical formulation are discussed.

* Correspondence and reprints

2. Analytical formulation of the wall shear stress

The conditions considered here correspond to Poiseuille bubbly flows in a circular cylindrical vertical duct (inner radius R). As in [1], the flow is co-current upward, steady, fully developped and axisymmetric. Mean phase velocities are parallel to the duct axis (z coordinate is along the vertical axis). The dispersed phase is composed of spherical bubbles of equal diameter d. The parameters characterising these two-phase flows are the Poiseuille number $P = \mu_L Q_L/(4\pi\rho_L g R^4)$ or equivalently the liquid Reynolds number $\mathrm{Re}_L = 2Q_L/(\pi\nu_L R)$, the gas flow rate ratio $\beta = Q_G/(Q_G + Q_L)$, the bubble radius scaled by the channel radius $\varepsilon = d/(2R)$, the particulate Reynolds number $\mathrm{Re}_p = d w_r/\nu_L$ where $w_r = w_G - w_L$ is the average relative axial velocity, and a parameter accounting for the interface contamination $\kappa = (\mu_G + \zeta)/\mu_L$, where ζ is a retardation coefficient.

The closure laws introduced are the same as in [1], and it is again assumed that the pseudo-turbulent stress is negligible compared to the average viscous stress. Using the same notation as in [1], except for the running space variable which is now the radial distance r to the duct axis, the axial momentum balance equations for both phases leads to:

$$G = \frac{36\phi_1\mu_L}{d^2} w_r, \tag{1}$$

$$(1-\alpha)\rho_L g - G = \mu_L(1-\alpha)\phi_0 \frac{1}{r}\frac{d}{dr}\left[r\frac{d}{dr}w_L\right]. \tag{2}$$

The above equations are then solved after introducing an idealised void fraction distribution in the form of a step function (*figure 1*). Rewriting equation (2) for each of the three layers, ones gets:

– for the one phase region close to wall ($\Delta_1 \leqslant r \leqslant R$):

$$\frac{d}{dr}\left[r\frac{d}{dr}w_L^{(1)}\right] = \frac{\rho_L g - G}{\mu_L} r \equiv s_1 r, \tag{3}$$

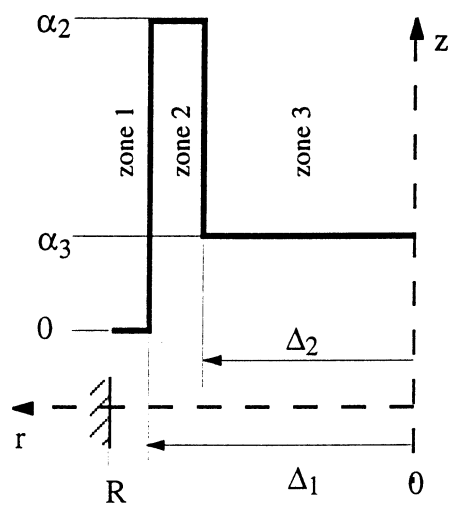

Figure 1. Idealised void fraction profile.

– for the two-phase flow regions 2 ($\Delta_2 \leqslant r \leqslant \Delta_1$) and 3 ($0 \leqslant r \leqslant \Delta_2$):

$$\frac{d}{dr}\left[r\frac{d}{dr}w_{\mathrm{L}}^{(n)}\right] = \frac{(1-\alpha_n)\rho_{\mathrm{L}}g - G}{\mu_{\mathrm{L}}(1-\alpha_n)\phi_0(\alpha_n)}r \equiv s_n r, \tag{4}$$

where $n = 2$ or 3. Since s_1, s_2 and s_3 are constant due to the step function imposed for the void fraction, equations (3) and (4) can be readily integrated to yield:

$$w_{\mathrm{L}}^{(n)} = s_n\frac{r^2}{4} + a_{n1}\ln r + a_{n2}, \tag{5}$$

where the coefficients a_{n1} and a_{n2} are determined from the boundary conditions which write:

– stick condition on the wall: $w_{\mathrm{L}}^{(1)} = 0$ at $r = R$,
– symmetry condition on the axis: $(d/dr)w_{\mathrm{L}}^{(3)} = 0$ at $r = 0$,
– continuity of velocities at the inner layers boundaries:

$$w_{\mathrm{L}}^{(1)} = w_{\mathrm{L}}^{(2)} \quad \text{at } r = \Delta_1 \quad \text{and} \quad w_{\mathrm{L}}^{(2)} = w_{\mathrm{L}}^{(3)} \quad \text{at } r = \Delta_2,$$

– continuity of tangential stress at the inner layers boundaries:

$$\frac{d}{dr}w_{\mathrm{L}}^{(1)} = (1-\alpha_2)\phi_0(\alpha_2)\frac{d}{dr}w_{\mathrm{L}}^{(2)} \quad \text{at } r = \Delta_1,$$

$$(1-\alpha_2)\phi_0(\alpha_2)\frac{d}{dr}w_{\mathrm{L}}^{(2)} = (1-\alpha_3)\phi_0(\alpha_3)\frac{d}{dr}w_{\mathrm{L}}^{(3)} \quad \text{at } r = \Delta_2.$$

Once the liquid profile is available, the evaluation of the total liquid flow rate, given by the integral of $(1-\alpha)w_{\mathrm{L}}$ over the pipe cross-section, provides an expression of the axial pressure gradient G versus the Poiseuille number, and the parameters defining the idealised void profiles, i.e. $\alpha_2, \alpha_3, \Delta_1, \Delta_2$. Let us introduce the width of the layers $\delta_1 = R - \Delta_1$ and $\delta_2 = R - \Delta_2$, and their dimensionless counterpart defined as $\delta_n^* = \delta_n/R$. As in [1], $b = \alpha_2/\alpha_3$ is the ratio of the void fraction at the peak to that in the core, and $a - 1 = (\delta_2 - \delta_1)/\delta_1$ is the ratio of the widths of the void peak layer to that of the single-phase flow layer. Then, G is found to be:

$$\frac{G}{\rho_{\mathrm{L}}g} = (1-\alpha_3)\frac{N}{D} + \frac{32P\phi_0^{(3)}}{D}, \tag{6}$$

where N and D, which depend on the parameters α_2, α_3, Δ_1, and Δ_2, are given in the Appendix in their complete form. Alternately, another very general expression for G is obtained by integrating over a tube section the complete form of the axial momentum balance for the liquid phase (see equation (12) in [1]):

$$\frac{G}{\rho_{\mathrm{L}}g} = 1 - \langle\alpha\rangle - \frac{2\tau_{\mathrm{w}}}{\rho_{\mathrm{L}}gR}, \tag{7}$$

where τ_{w} is the wall friction and where the surface gas fraction $\langle\alpha\rangle$ is given by:

$$\langle\alpha\rangle = \frac{2\pi}{\pi R^2}\int_0^R \alpha(r)r\,dr. \tag{8}$$

For the idealised void profile of *figure 1*, ones gets:

$$\langle\alpha\rangle = \alpha_3\left\{1 + 2\delta_1^*[(a-1)(b-1)-1] + \delta_1^{*2}\left(a^2(1-b)+b\right)\right\}. \tag{9}$$

Hence, replacing the expressions (6) for G and (9) for $\langle\alpha\rangle$ in equation (7), the wall friction is established. Scaled by the wall shear stress $\tau_{w0} = -16\rho_L g R P$ which occurs in single-phase conditions at the same liquid flow rate, it becomes:

$$\frac{\tau_w}{\tau_{w0}} = \frac{\phi_0^{(3)}}{D} + \frac{1}{32P}\left[(1-\alpha_3)\left(\frac{N}{D}-1\right) + \langle\alpha\rangle - \alpha_3\right]. \tag{10}$$

This equation is identical to that obtained for plane flows (see equation (28) in [1]) except for the coefficient 32 in place of 12. Setting the function $\phi_0(\alpha)$ to $(1-\alpha)^{-1}$, which is an exact closure for solid particles or for contaminated bubbles (see [1]), the complete expression (10) takes a very simple form when the widths δ_1 and δ_2 are much smaller than the duct radius. Indeed, at the order one in δ_1^*, $N = 1 + O(\delta_1^{*2})$ and $D = 1 + O(\delta_1^{*2})$, so that one gets:

$$\begin{aligned}\frac{\tau_w}{\tau_{w0}} &= \frac{1}{1-\alpha_3} + \frac{\alpha_3\delta_1^*}{16P}(-a-b+ab) + O(\delta_1^{*2}) \\ &= \frac{1}{1-\alpha_3} + \frac{\alpha_3\delta_1^*}{16P}[(a-1)(b-1)-1] + O(\delta_1^{*2}).\end{aligned} \tag{11}$$

As for plane Poiseuille bubbly flows, the parameters connected with the void profile which control the friction are the core void fraction α_3, the width δ_1^* of the single-phase layer close to walls and the gas excess in the void peak represented by $(a-1)(b-1)$. Note that the latter quantity can corresponds as well to a gas deficiency. The equation (11), being quite similar to the expressions obtained in plane flows (see equations (31), (32) in [1]), the behaviour of the τ_w/τ_{w0} ratio with the structure of the void profile is not discussed again here. Emphasis is now put on experimental results before analysing the validity of the formula (10) and (11).

3. Experimental data

3.1. Experimental set-up and measuring techniques

Experiments were performed on the set-up described in Kashinsky et al. [2]. The test section is a 14.8 mm i.d. and 6.5 m long stainless steel pipe. Air is injected at the bottom of the tube through a mixer. Two types of air injectors were used in order to vary the bubble size. The first one, made of stainless steel, is a 29 mm outer diameter and 32 mm long cylinder. It is composed of two metallic rings with polished front surfaces. Radial grooves 50 μm deep were machined on the surface of one ring, while the other one was left smooth. When placed face to face, the grooves form channels through which air was injected into the flow. This injector will be referred to as M-injector. The second one, made of plexiglass and thus called P-injector, is a cylinder 32 mm outer diameter in which 18 holes of 0.15 mm inner diameter were drilled: air was injected into the flow through these holes. The mean bubble sizes were determined in the measuring section by photography: the mean diameters are typically equal to 1.3 mm for the M-injector and to 2.2 mm for the P-injector (precise values are given in *table I*), and the dispersion from the mean is usually less than $\pm 15\%$. Hence, ε is about 0.09 for the M-injector and 0.15 for the P-injector.

The test liquid was a solution of 0.005 N potassium ferro- and ferricyanide and 0.25 M sodium hydroxide in distilled water. In order to increase the viscosity of the test liquid, glycerine was added to the solution. The temperature of the liquid was maintained constant at 20 ± 0.2°C by an automatic controller. Note that the temperature level was the same during probe calibration and during the experiments. The kinematic viscosity of the liquid at this temperature is 10×10^{-6} m^2/s and its density 1169 kg/m^3. The assumption that the bubbles are strongly contaminated in such a test liquid, which is a strongly ionic solution, needs to be checked. The

Table I. Flow conditions and some characteristics of the experimental void profiles.

P-injector	Re_L	P	d (mm)	ε	δ_1^*	Δ peak (mm)	α peak (%)	Re_p^*
$\beta = 0.02$	106	3.30E−04	2.2	0.15	0.270	-	-	28
	300	9.30E−04	2.1	0.14	0.068	-	-	25
	562	1.75E−03	1.5	0.10	0.101	-	-	polydispersed
	980	3.05E−03	1.3	0.09	0.135	-	-	5
$\beta = 0.1$	20	6.20E−05	2.3	0.16	0.169	-	-	30
	106	3.30E−04	2.1	0.14	0.095	4.5	6.3	24
	300	9.30E−04	2.4	0.16	0.074	4.6	10.0	34
	562	1.75E−03	2.3	0.16	0.074	3.7	10.7	27
	980	3.05E−03	1.3	0.09	0.061	2.4	13.5	5
$\beta = 0.2$	11.4	3.50E−05	1.9	0.13	0.135	-	-	19
	106	3.30E−04	2.1	0.14	0.054	4.9	14.8	23
	300	9.30E−04	2.2	0.15	0.047	4.8	22.9	25
	562	1.75E−03	1.9	0.13	0.074	3.4	22.8	14

M-injector	Re_L	P	d (mm)	ε	δ_1^*	δ peak (mm)	α peak (%)	Re_p^*
$\beta = 0.02$	300	9.30E−04	1.4	0.09	0.074	5.8	8.1	6
	562	1.75E−03	1.3	0.09	0.061	5.3	4.8	6
	980	3.05E−03	0.7	0.05	0.034	-	-	polydispersed
$\beta = 0.1$	20	6.20E−05	1.2	0.08	0.135	4.6	3.0	5
	48	1.50E−04	1.0	0.07	0.061	5.9	5.4	6
	300	9.30E−04	1.2	0.08	0.027	6.2	18.7	6
	562	1.75E−03	1.4	0.09	0.020	5.7	19.3	6
	980	3.05E−03	1.4	0.09	0.020	-	-	6
$\beta = 0.2$	11.4	3.50E−05	1.3	0.09	0.088	4.6	3.3	5
	48	1.50E−04	1.4	0.09	0.054	5.4	12.0	5
	300	9.30E−04	1.5	0.10	0.014	6.0	29.0	6
	562	1.75E−03	1.5	0.10	0.014	5.8	28.1	6

terminal velocity of isolated bubbles w_t was measured in an infinite liquid. Its composition was the same as that of the test liquid, except for a reduction in the proportion of glycerol which leads to a kinematic viscosity $\nu_L = 3.5 \times 10^{-6}$ m^2/s. For bubbles with a diameter between 1 and 3.2 mm, the experimental correlation was $w_t = 40.45 d^{0.904}$. When varying the diameter from 1 to 3 mm, the Re_p varies from 22 to 180 and the drag coefficient $C_D = 4gd/(3w_t^2)$ from 2.2 to 0.87. These values are close to those obtained for solid spheres using the following correlation given in Clift et al. [3]: $C_D = (24/Re_p)(1 + 0.1935 Re_p^{0.6235})$, for $20 < Re_p < 260$. On the other hand, the drag coefficients (Clift et al. [3]) for bubbles without any contamination are significantly lower: C_D evolves between 1.4 and 0.27 for Re_p between 20 and 200. Thus, the assumption that bubbles are strongly contaminated seems reasonable.

The section where void fraction profiles and wall shear stress are measured is located 5.25 metres, i.e. more than 350 pipe diameter, downstream from the injection. The flow development was not checked in these experiments. Nevertheless, in a downward bubbly flow with the same test liquid and a pipe diameter of 42 mm (Kashinsky and Randin [4]), the flow was stabilised after 50 diameters. Then, it will be considered in the sequel that the flow was fully developed, as it is assumed in the model.

Wall shear stress measurements were performed using an electrodiffusional technique (Nakoryakov et al. [5, 6]) which is based on the quantification of the rate of mass transfer from a microelectrode to the liquid.

The probe is a 100×700 μm cross section platinum foil embedded into the wall and polished flush with it. Its smaller dimension is normal to the flow direction. The probe current is amplified by a DC amplifier and then digitised and processed by a computer. The relation between the probe current and the wall shear stress is established from a calibration performed in single-phase laminar flows in the same pipe. In practice, a measuring unit containing eight wall shear stress probes was used. The probes were arranged uniformly over the pipe circumference. Moreover, in order to obtain the direction of the wall shear stress, a double wall probe was also used (Nakoryakov et al. [5]). Accuracy on wall friction is estimated to be $\pm 7\%$. Local void fraction measurements were obtained from a conductivity technique. The probe consists of a 20 μm diameter platinum wire welded into a conical glass capillary. The outer diameter of the probe at the working tip is about 50 μm. In order to measure void profiles, the probe was traversed from the wall to the pipe centre by a traversing mechanism with a step about 0.1 mm. The raw signal from the probe was processed by a home-made analog device to obtain the local void fraction. Its accuracy is typically $\pm 20\%$ (Nakoryakov et al. [6]).

3.2. Void fraction measurements

Void fraction profiles were measured at different liquid velocities corresponding to Poiseuille numbers between 3.5×10^{-5} and 1.77×10^{-3} or liquid Reynolds numbers ranging from 10 to 1000, and for gas flow rate ratios β equal to 0.02, 0.1 and 0.2. The mean bubble diameter is given in *table I* for the flow conditions investigated. No measurements have been made of the interface contamination nor on actual relative velocities. Assuming that bubbles are strongly contaminated, an estimate of the particulate Reynolds number (noted Re_p^*) is given in *table I* which is based on the Stokes drag law and on the pressure gradient G calculated from equation (7), without taking into account of any hindering effect. Typically, Re_p^* ranges from 40 to 70 for the P-injector and from 5 to 18 for the M-injector. For some conditions, the bubble size distribution was polydispersed; these are also indicated in (*table II*).

Table II. Characterisation of the idealised void profiles.

P-injector	$\mathrm{Re_L}$	α_3 (%)	δ_2^*	α_2 (%)	$\delta_2'^*$	a	b	$(a-1)(b-1)$
$\beta = 0.1$	106	3.5	0.595	3.84	0.401	4.24	1.10	0.31
	300	4.6	0.649	6.08	0.423	5.69	1.32	1.51
	562	6.5	0.784	6.63	0.516	6.95	1.02	0.12
$\beta = 0.2$	106	7.8	0.527	8.95	0.341	6.31	1.15	0.78
	300	11.0	0.581	13.60	0.343	7.30	1.24	1.49
	562	17.0	0.730	13.90	0.473	6.36	0.18	−0.96

M-injector	$\mathrm{Re_L}$	α_3 (%)	δ_2^*	α_2 (%)	$\delta_2'^*$	a	b	$(a-1)(b-1)$
$\beta = 0.02$	300	0.1	0.284	4.05	0.176	2.37	57.86	78.12
	562	0.22*	0.473	2.44	0.268	4.39	11.09	34.17
$\beta = 0.1$	20	1.5	0.419	1.58	0.288	2.13	1.05	0.06
	48	2.8*	0.311	3.33	0.220	3.61	1.19	0.49
	300	3.5	0.297	10.20	0.168	6.21	2.91	9.97
	562	4*	0.405	10.50	0.227	11.24	2.63	16.64
$\beta = 0.2$	11.4	1.9	0.459	1.86	0.297	3.38	0.98	−0.05
	48	6.0	0.500	7.48	0.323	5.98	1.25	1.23
	300	10.0	0.311	16.50	0.184	13.61	1.65	8.20
	562	10.0	0.378	16.20	0.222	16.42	1.62	9.56

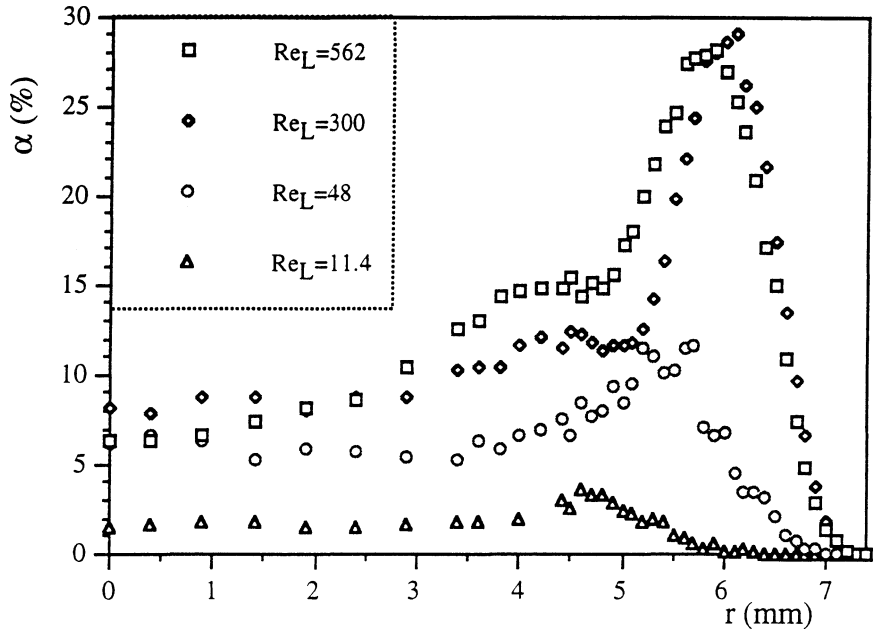

Figure 2. Experimental void profiles for $\beta = 0.2$, M-injector, $\nu_L = 10 \times 10^{-6}$ m^2/s.

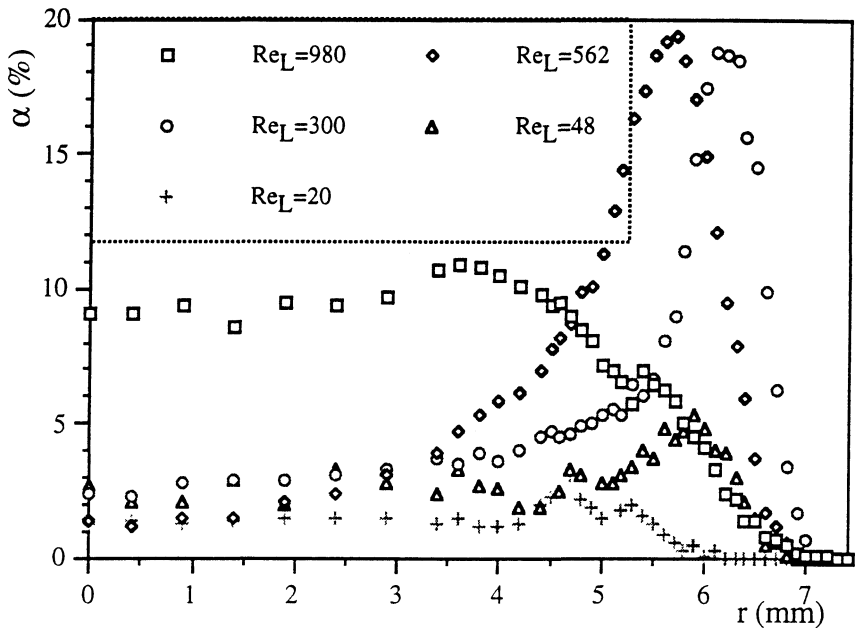

Figure 3. Experimental void profiles for $\beta = 0.1$, M-injector, $\nu_L = 10 \times 10^{-6}$ m^2/s.

Void fraction profiles are given in *figures 2* to *7*. Each of these figures presents data for the same gas flow rate ratio β, the same injector, but for different values of Re_L. Clearly, the shape of the void profile depends significantly on the flow parameters. In most cases, the void fraction is almost flat in the core of the flow except for $Re_p = 600$ where the void fraction is continuously decreasing when approaching the duct axis. A second

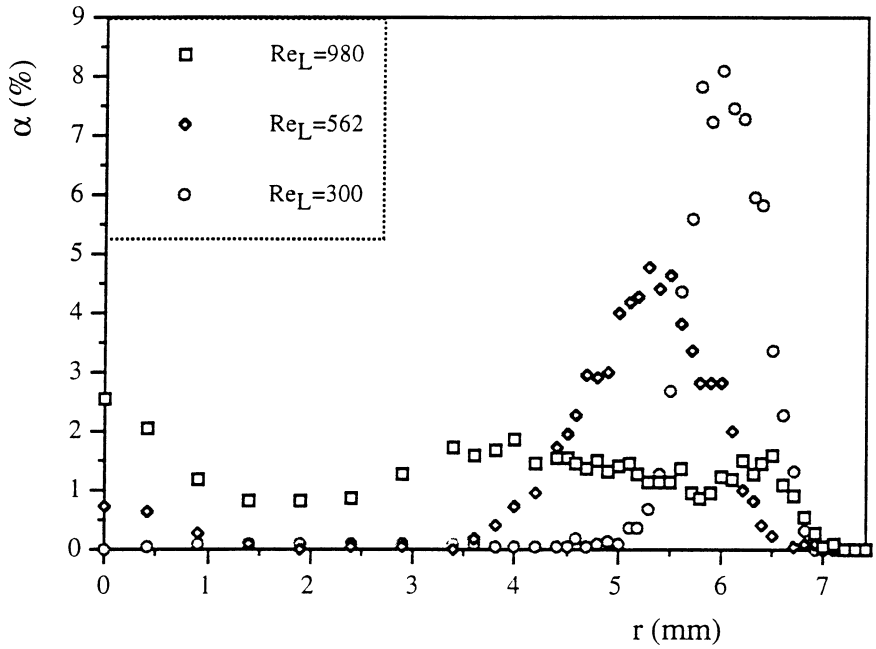

Figure 4. Experimental void profiles for $\beta = 0.02$, M-injector, $\nu_L = 10 \times 10^{-6}$ m^2/s.

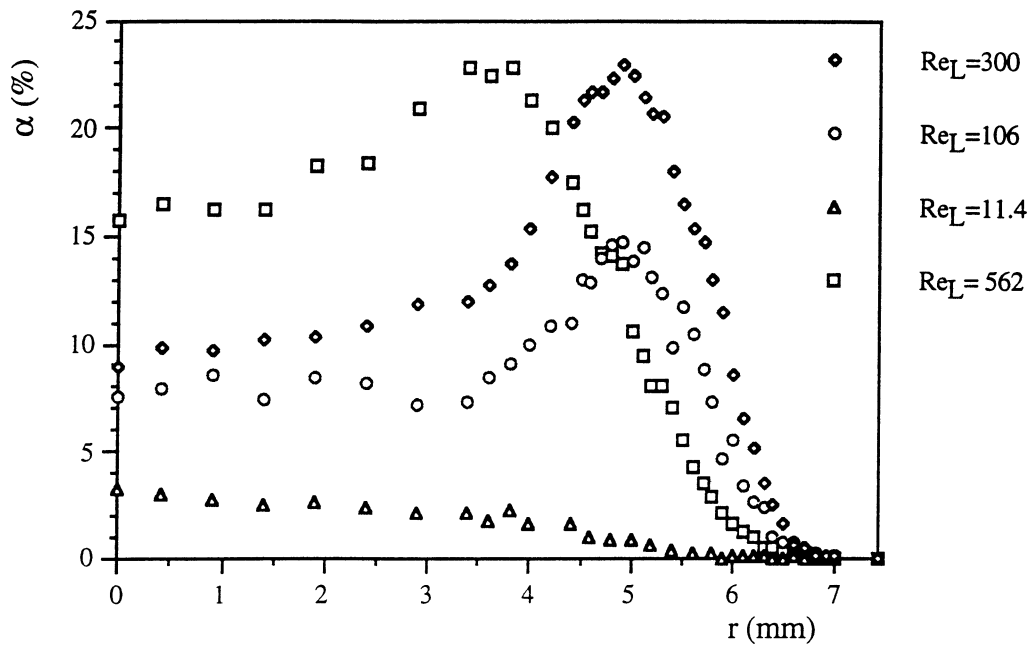

Figure 5. Experimental void profiles for $\beta = 0.2$, P-injector, $\nu_L = 10 \times 10^{-6}$ m^2/s.

common feature is that, whatever the injector considered, wall peaking is absent at low liquid Reynolds number, say below 20. By increasing the liquid velocity, the wall void peak appears systematically: it growths steadily up to $Re_p = 300$. With a further increase of the liquid velocity, the void peak widens while its maximum shifts

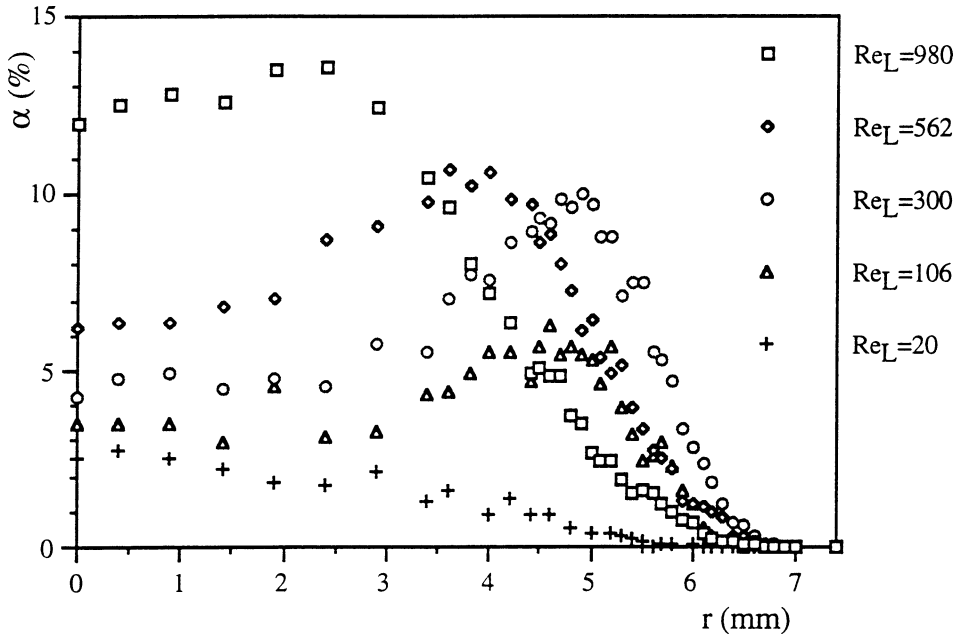

Figure 6. Experimental void profiles for $\beta = 0.1$, P-injector, $\nu_L = 10 \times 10^{-6}$ m^2/s.

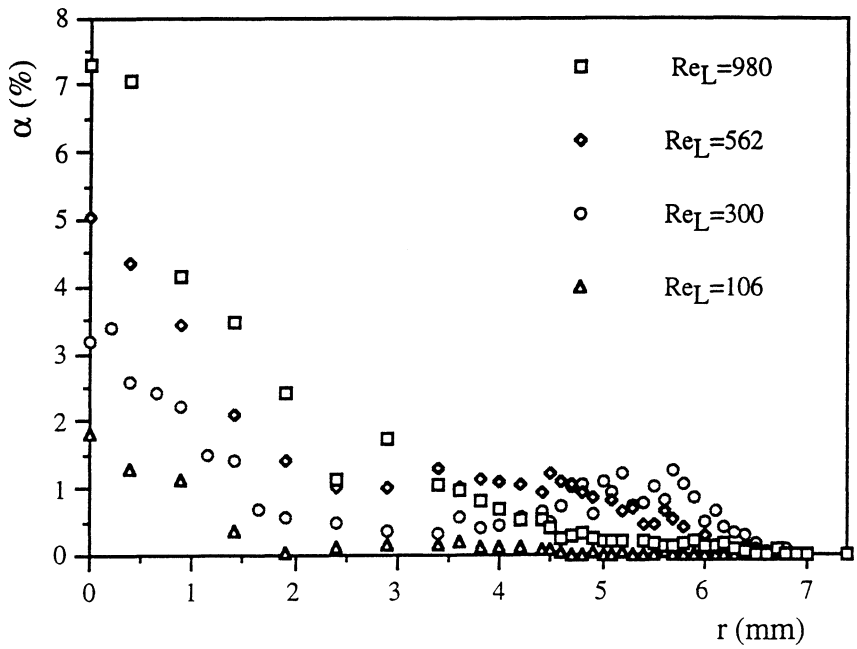

Figure 7. Experimental void profiles for $\beta = 0.02$, P-injector, $\nu_L = 10 \times 10^{-6}$ m^2/s.

toward the duct axis (see *table I*). For the highest liquid velocity investigated, namely for $Re_L = 1000$, the peak almost completely diffuses, the void profile becomes nearly uniform, except for a region close to the wall whose extent varies according to the injector considered. Besides, the void fraction at the peak α_p increases continuously with β (see *table I*). Meanwhile, the void fraction in the core depends both on Re_L and on β,

and it varies greatly with the bubble size: for the smallest bubbles (M-injector), it is close to zero for $\beta = 0.02$ and $\mathrm{Re_L} = 300$ and 600, indicating that an almost complete migration of the bubbles from the central region to the wall void peak had occured. On the other hand, for the largest bubbles (P-injector), the void fraction in the core never approaches zero. Globally, the profiles for the P-injector are less pronounced than those for the M-injector: this effect is connected with the increase of the mean bubble size and probably also with some departure from sphericity. However, a near-wall void peak exists for $\mathrm{Re_L}$ in the range 100 to 600 and for $\beta = 0.1$ and 0.2. The peak is more distant from the wall because of the larger bubble diameter. Let us also mention that the profiles obtained with the P-injector at low gas fraction $\beta = 0.02$ are singular. Indeed, for all liquid Reynolds numbers, strong void coring occurs. Besides, a weak wall peak can only be seen for $\mathrm{Re_L} = 300$, perhaps due to the coexistence of two main bubble diameters for these specific conditions. Such features have been already observed on almost the same experimental conditions but with well marked void peaking and void coring at the same time (see figure 10 in Kashinsky et al. [2]). A small amount of coring can be also perceived at $\beta = 0.02$ for smaller bubbles produced by the M-injector (*figure 4*). Visual observation does not indicate any formation of clusters, which are known to produce void coring (Cartellier et al. [7]). Hence, the explanation for such a void distribution is left open: it may be due to a non-symmetrical distribution inside the cross section eventually favoured by a slight deformation of bubbles (not all of them being perfectly spherical for the P-injector), or else to a strong wall repulsion force whose role is favoured by the high ε value (here not less than 0.1).

A last common feature of these experimental data is the presence of a near wall region free of gas ($\alpha = 0$). It exists for all flow conditions, but its width δ_1 evolves from 0.1 to 0.7 mm in presence of a well marked peak, and it can reach 1.5 mm in presence of void coring. The evolution of δ_1^* versus $\mathrm{Re_L}$ and β is plotted in *figure 8* (see also *table I*): whenever wall peaking is present, δ_1^* is less than 10% and it can be as small as 2%. Hence, for most of the experimental conditions investigated, the clear fluid layer is small enough compared to the pipe radius to allow the use of the simplified formula (10). Let us also remark that, except for the case

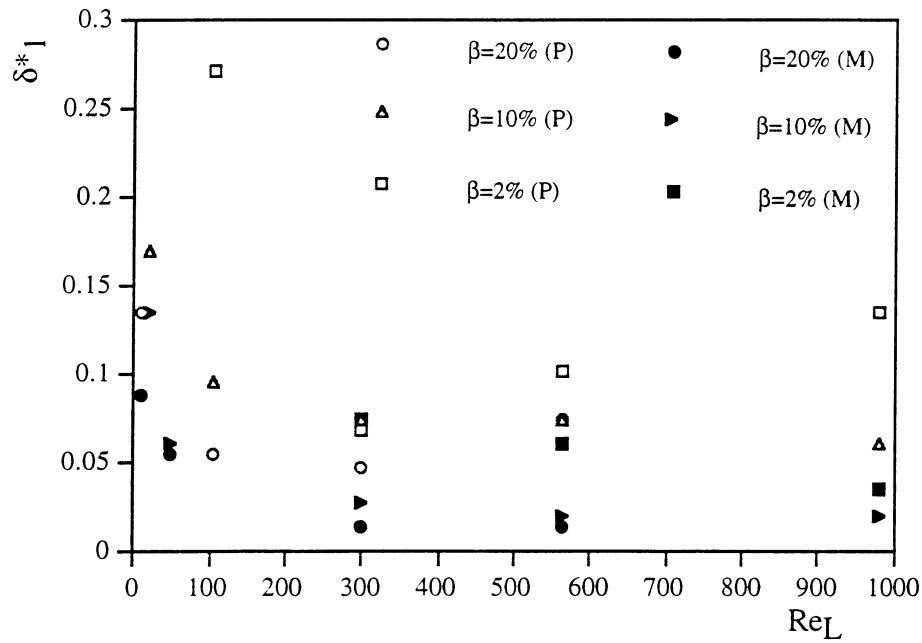

Figure 8. Dimensionless clear fluid layer thickness δ_1^* versus flow conditions ($\nu_\mathrm{L} = 10 \times 10^{-6}$ m^2/s).

$Re_L = 106$, $\beta = 0.02$, P-injector, its width δ_1 is always less than one bubble radius, so that the scaling $\delta_1^* \approx \varepsilon$ used in section 2.4 of [1] is reasonable.

3.3. Wall shear stress measurements

Mean cross-sectional wall shear stress values, i.e. averaged over the eight probes, were measured at different flow regimes obtained by varying Re_L at $\beta = 0.02$, 0.1 and 0.2 and for both injectors. Results are presented as the ratio of the two-phase wall shear stress to the single-phase one evaluated at the same liquid velocity, versus Re_L (*figures 9* and *10*).

For the bubbles obtained with the P-injector, where the diameter is above 2 mm, τ_w/τ_{w0} remains close to unity for a wide range of liquid Reynolds numbers. A similar behaviour was obtained at a viscosity of $\nu_L = 7.02 \times 10^{-6}$ m^2/s with the same injector (Kashinsky et al. [2]). However, at $\nu_L = 3.5 \times 10^{-6}$ m^2/s, and again for the same injector, larger τ_w/τ_{w0} ratios, up to 2 have been recorded (Kashinsky et al. [8]).

For the M-injector, which produces smaller bubble diameter, *figure 10* shows that τ_w/τ_{w0} is higher than unity for most flow conditions: such a behaviour has been already observed with the same injector for two other viscosities of the liquid phase namely $\nu_L = 7.02 \times 10^{-6}$ m^2/s (Kashinsky et al. [2]) and at $\nu_L = 3.5 \times 10^{-6}$ m^2/s (Kashinsky et al. [8]). The highest τ_w/τ_{w0} ratios are fairly large: they evolve between 2 to 4. A general trend is also that the ratio τ_w/τ_{w0} approaches unity as Re_L gets close to 1000.

These features clearly indicate that the bubble dynamics has an essential role on the evolution of the shear stress. Unfortunately, the particulate Reynolds numbers associated with these experiments are rarely available, mainly because reliable measurements of actual relative velocities are not easy. Hence, the connection between wall shear stress and Re_p cannot be analysed in detail.

A second interesting feature of *figures 9* and *10*, is that negative τ_w/τ_{w0} ratios are registered for significant gas flow rate fractions ($\beta = 0.1$ and 0.2), provided that the liquid Reynolds number is low enough, namely

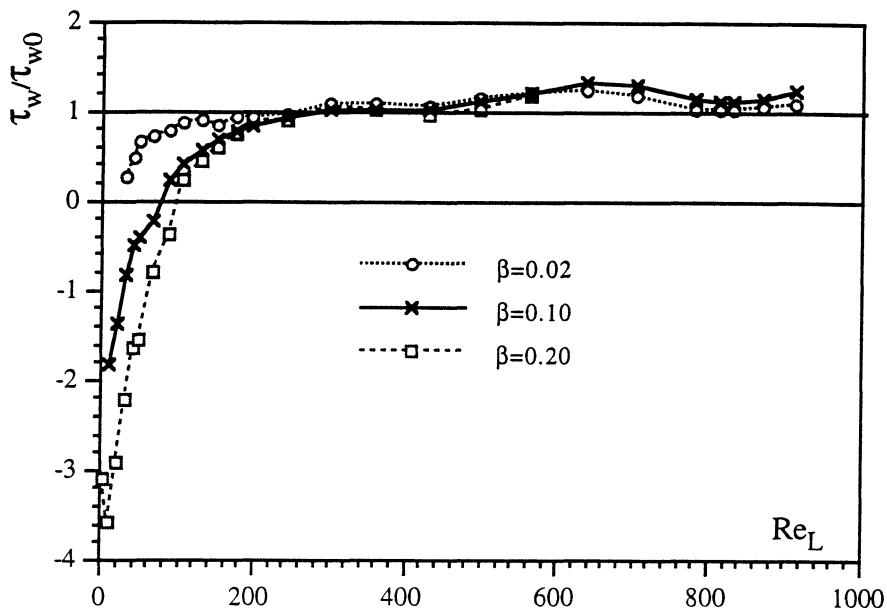

Figure 9. Ratio of the average wall shear stress in two-phase flow to the single phase wall friction at the same liquid flow rate versus Re_L at various β (P-injector, $\nu_L = 10 \times 10^{-6}$ m^2/s).

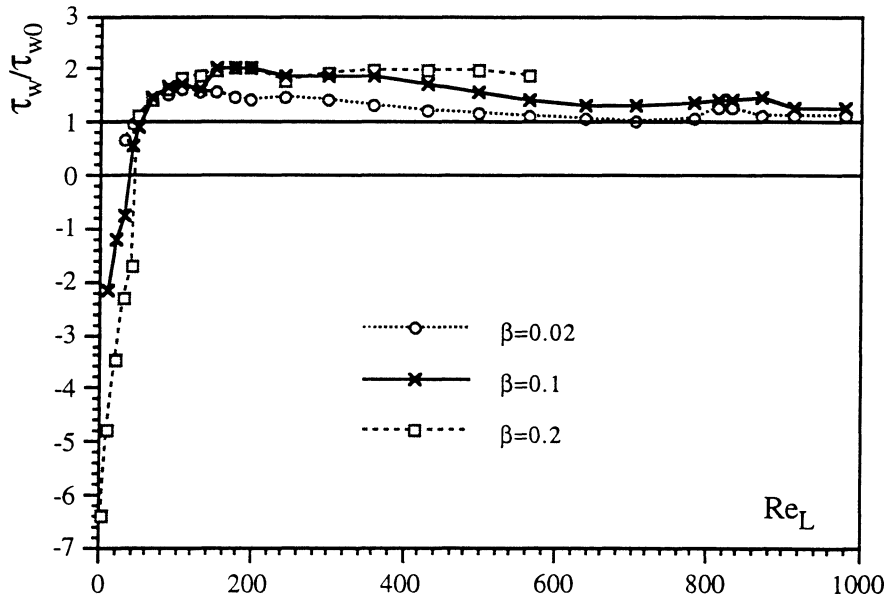

Figure 10. Ratio of the average wall shear stress in two-phase flow to the single phase wall friction at the same liquid flow rate versus Re_L at various β (M-injector, $\nu_L = 10 \times 10^{-6}$ m^2/s).

$Re_L < 100$ for P-injector and $Re_L < 50$ for the M-injector. Negative τ_w/τ_{w0} ratios correspond to a bubble-driven liquid circulation which induces a liquid downflow near the wall: such features have been observed in a channel by Cartellier et al. [9] and in the same duct at a lower liquid viscosity ($\nu_L = 3.5 \times 10^{-6}$ m^2/s, $\rho_L = 1127$ kg/m^3) (Kashinsky et al. [8,10]). Their onset has already been discussed and compared to experiments in [1]. Let us note that at the lowest gas flow rate fraction $\beta = 0.02$, backflows have not been observed because, in these conditions, the bubble arrival frequency is less than 0.1 Hz: the two-phase flow is thus composed of well separated, i.e. almost isolated bubbles.

So far, the mean value of the wall shear stress has been considered. Since eight probes were installed around a tube perimeter, the angular distribution of the stress is accessible. An example of such a distribution is given *figure 11* for the M-injector at $\beta = 0.1$; the quantity plotted is τ_w/τ_{w0}. The uneven distribution of the friction at low liquid Reynolds numbers is striking. It occurs not only for downward flows but also for all conditions for which the friction is lower than its single-phase flow equivalent. Similar behaviours were observed for all the flow conditions investigated. To illustrate this point, the difference between the highest and the lowest measurements scaled by the mean value of the friction has been plotted *figures 12* and *13* for the P and M injectors, respectively. Roughly, the symmetry is broken for Re_L below 200 to 250 whatever the flow conditions, and besides, the asymmetry drastically increases at small Re_L. For these flow conditions, the model presented in section 2 is expected to be invalid.

4. Comparison with predictions

The model developed in section 2 is now used to evaluate the wall shear stress values for various flow regimes. The comparison between predicted and measured wall friction can be performed only when void profiles are available since equations (10) or (11) require as inputs various characteristics of the void distribution. Hence, this comparison has been achieved for the flow conditions indicated in *table I*. The difficulty is now to define an idealised void profile which approximates correctly the experimental data, so that α_3, α_2, δ_1,

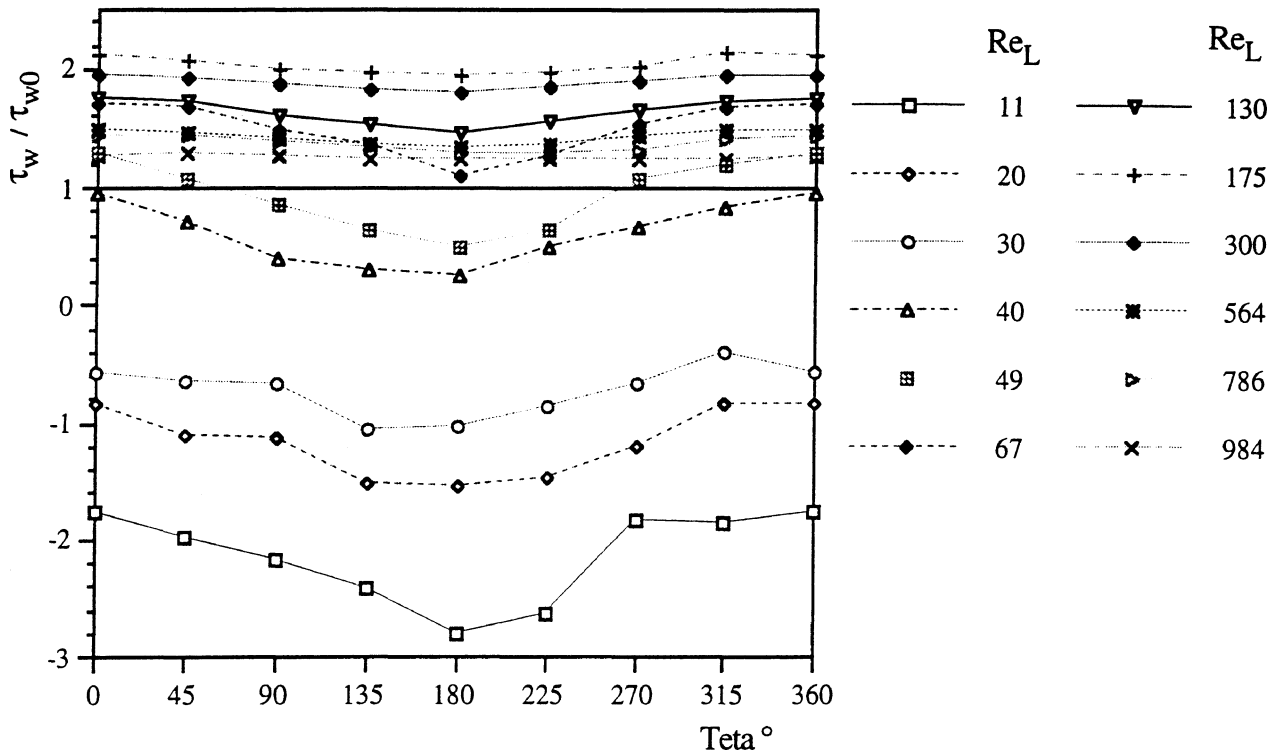

Figure 11. Example of angular distribution of the wall friction ($\beta = 0.1$, M-injector, $\nu_L = 10 \times 10^{-6}$ m^2/s).

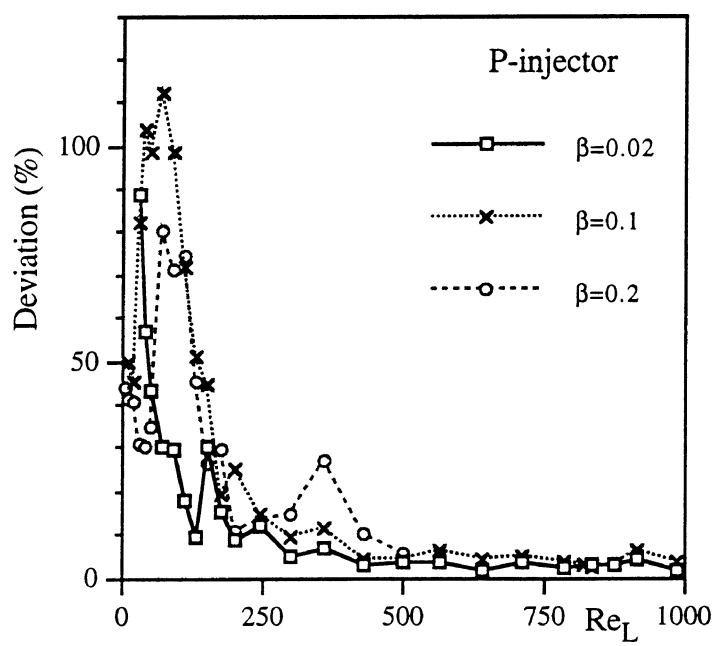

Figure 12. Maximum deviation of the wall shear stress along a duct perimeter for the P-injector, $\nu_L = 10 \times 10^{-6}$ m^2/s.

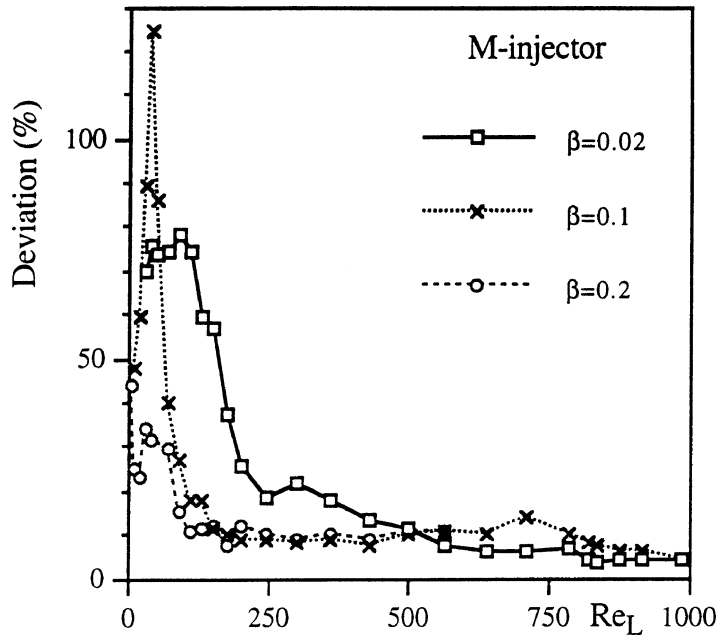

Figure 13. Maximum deviation of the wall shear stress along a duct perimeter for the M-injector, $\nu_L = 10 \times 10^{-6}$ m^2/s.

and δ_2 can be quantified. Clearly, such a process can be achieved for any type of profile, in which case the general formula (10) must be used. However, it is worthwhile to check first the simplified expression (11) which is well adapted to handle void peaking effects.

4.1. Void peaking regimes

Let us consider profiles exhibiting a void peak near the wall and an almost constant void fraction in the core. First of all, the determination of the clear fluid layer is unambiguous, and the values of δ_1^* given in *table I*, which have been determined as the first radial position from the wall where bubbles are detected, are kept. Besides, the determination of the location Δ_p and the amplitude α_p of the void peak are not ambiguous provided that enough data have been collected to provide a detailed description of the profile: they are also given in *table I*.

The definition of the remaining parameters is slightly more subjective. At this point, let us first underline that we seek to approximate the single variable function $\alpha(r)$ as a step function: there is thus no need to take into account the geometry of the duct which has already been accounted for by the model during the evaluation of the liquid flow rate and that of the mean gas fraction. Accordingly, α_3 is taken as the average of the almost constant part of the profile. For the determination of the idealised wall peak, various procedures can be imagined. Two are explained now.

First, the location of the transition between the zones 2 and 3, i.e. Δ_2 is defined by the intersection of α_3 with the line M_2M_p based on the slope of the wall peak, as indicated in *figure 14*. To define α_2, we choose to respect the area under the peak for $\Delta_2 \leqslant r \leqslant \Delta_1$, so that:

$$\alpha_2(\Delta_1 - \Delta_2) = \int_{\Delta_1}^{\Delta_2} \alpha(r)\, dr. \tag{12}$$

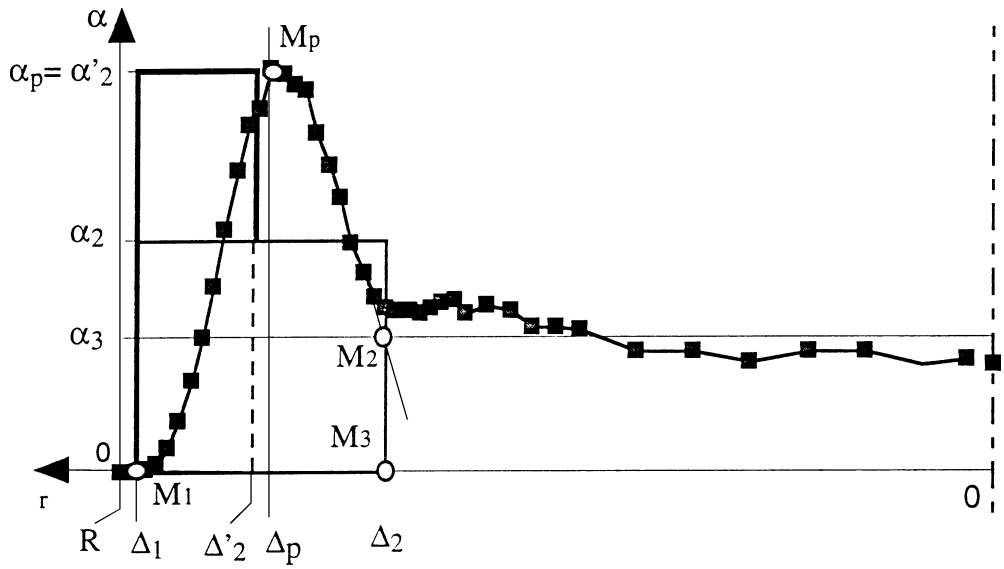

Figure 14. Illustration step function fits of an experimental void fraction distribution ($Re_L = 300$; $\beta = 0.2$; M-injector, $\nu_L = 10 \times 10^{-6}$ m^2/s).

For practical purposes, to evaluate the integral in equation (12), the void peak has been approximated as a triangular function defined by the segments M_pM_1 and M_2M_p. This procedure leads to the rectangle drawn in thin line in *figure 14*. The peak width is respected but not its amplitude which is significantly reduced.

A second procedure can be proposed which respects the gas excess in the peak. Hence, the void fraction α_2' in the zone 2 is equated to α_p, and the new boundary of the zone 2, noted Δ_2' is obtained according to:

$$(\alpha_p - \alpha_3)(\Delta_1 - \Delta_2') = \int_{\Delta_1}^{\Delta_2} [\alpha(r) - \alpha_3]\, dr. \tag{13}$$

This procedure corresponds to the rectangle in bold line in *figure 14*. Note that since the parameter $(a-1)(b-1)$ is the same for the two procedures, the predictions from the simplified formula (11) will be identical, but not those obtained with the complete equation (10).

The parameters α_3, Δ_1^*, a and b defining the idealised profiles issued from the above procedures are indicated in *table II*. Inserting these parameters in equation (10) or (11) provides estimates of the wall shear stress which are compared to the experimental values in *figures 15* and *16* for the M and P injectors, respectively. The predictions of equation (11) are given for $\phi_0 = (1-\alpha)^{-1}$. Let us remark that the closure proposed by Ryskin [11] for high particulate Reynolds numbers, which writes $\phi_0 = 1 + 5\alpha/3$, provides almost identical results.

As shown by *figures 15* and *16*, the simplified equation (11) is most often inaccurate: this is not surprising since equation (11) is valid when void peaks are narrow while their actual size is never less than 20% of the duct radius and can even reach 70% for some conditions. The complete expression (10) provides a much better estimate of the actual friction, and these predictions are weakly sensitive to the procedure chosen to fit the experimental void profiles. The agreement is fairly good over a wide range of Re_L, of β and for both injectors, but significant discrepancies occur at very low liquid Reynolds numbers (say below 20) where the positive friction is strongly underestimated. As mentioned at the end of section 3.3, such flow conditions correspond to strongly asymmetrical structures which are not accounted for by the model. Besides, the void profiles presented in section 3.2 have been collected along a given radius, and could be poorly representative of the actual gas

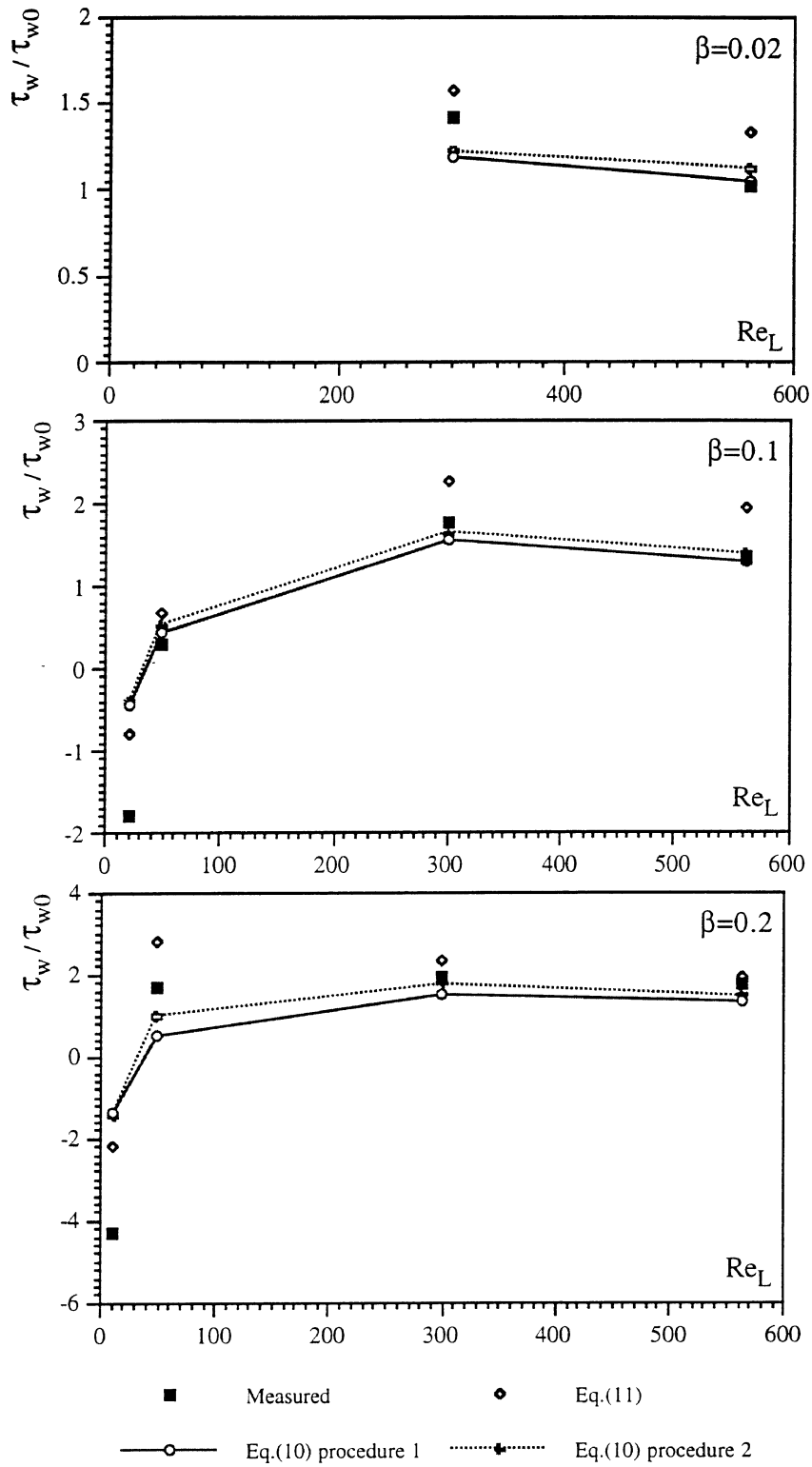

Figure 15. Comparison of predicted and measured values of τ_w/τ_{w0} (M-injector, $\nu_L = 10 \times 10^{-6}$ m^2/s).

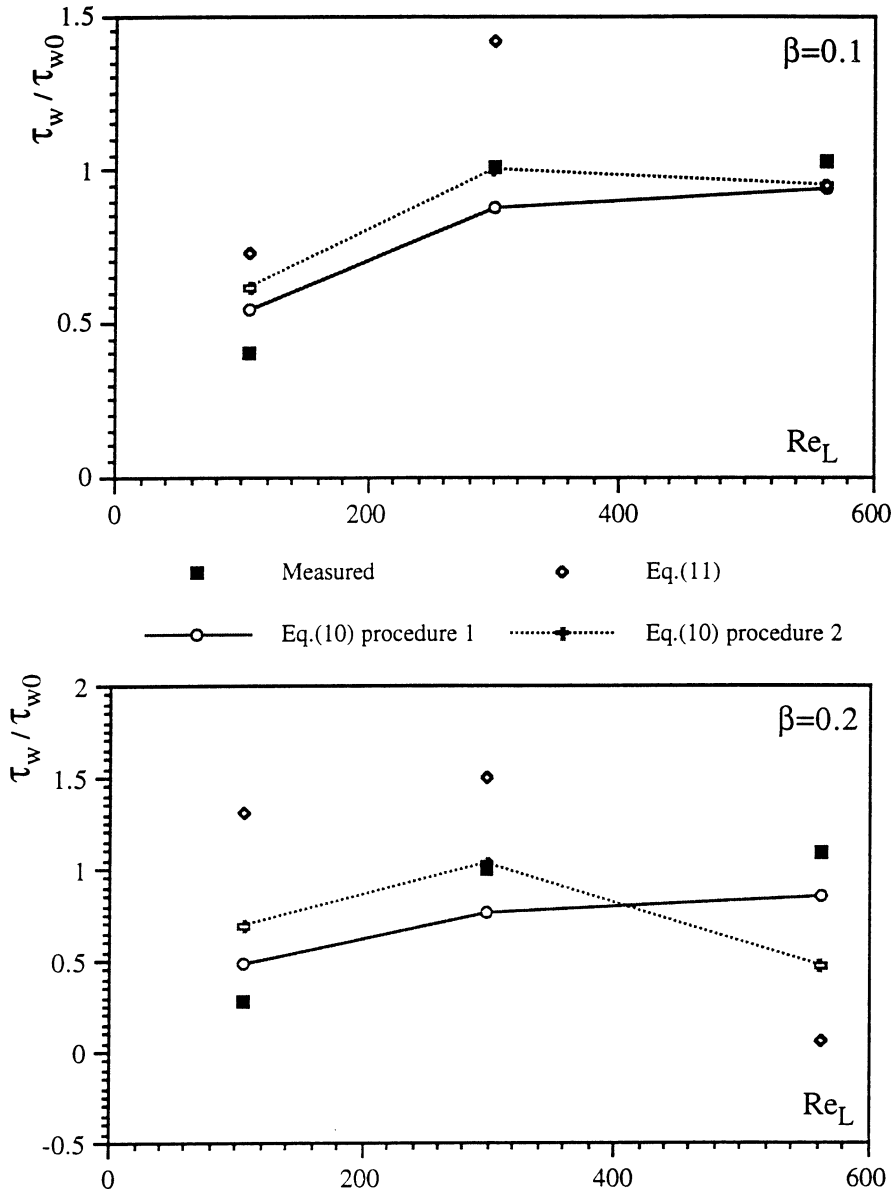

Figure 16. Comparison of predicted and measured values of τ_w/τ_{w0} (P-injector, $\nu_L = 10 \times 10^{-6}$ m^2/s).

distribution which is probably subject to large angular variations. For these reasons, the comparison between measured and calculated wall frictions is probably not significant in such cases.

Globally, the predictions are better for the M-injector than for the P-injector. This trend is connected with the increase of the bubble size, so that the void gradients obtained with the P-injectors are smoother than those produced with the M-injector. Therefore, the approximation of an actual void profile by a step-function becomes less valid. Some improvement can be expected using a step-function with multiple layers.

The model was also checked against experiments performed at a lower liquid viscosity ($\nu_L = 3.5 \times 10^{-6}$ m^2/s, $\rho_L = 1127$ kg/m^3). The void profiles obtained with the M-injector, were taken form Kashinsky et al. [8,12] and

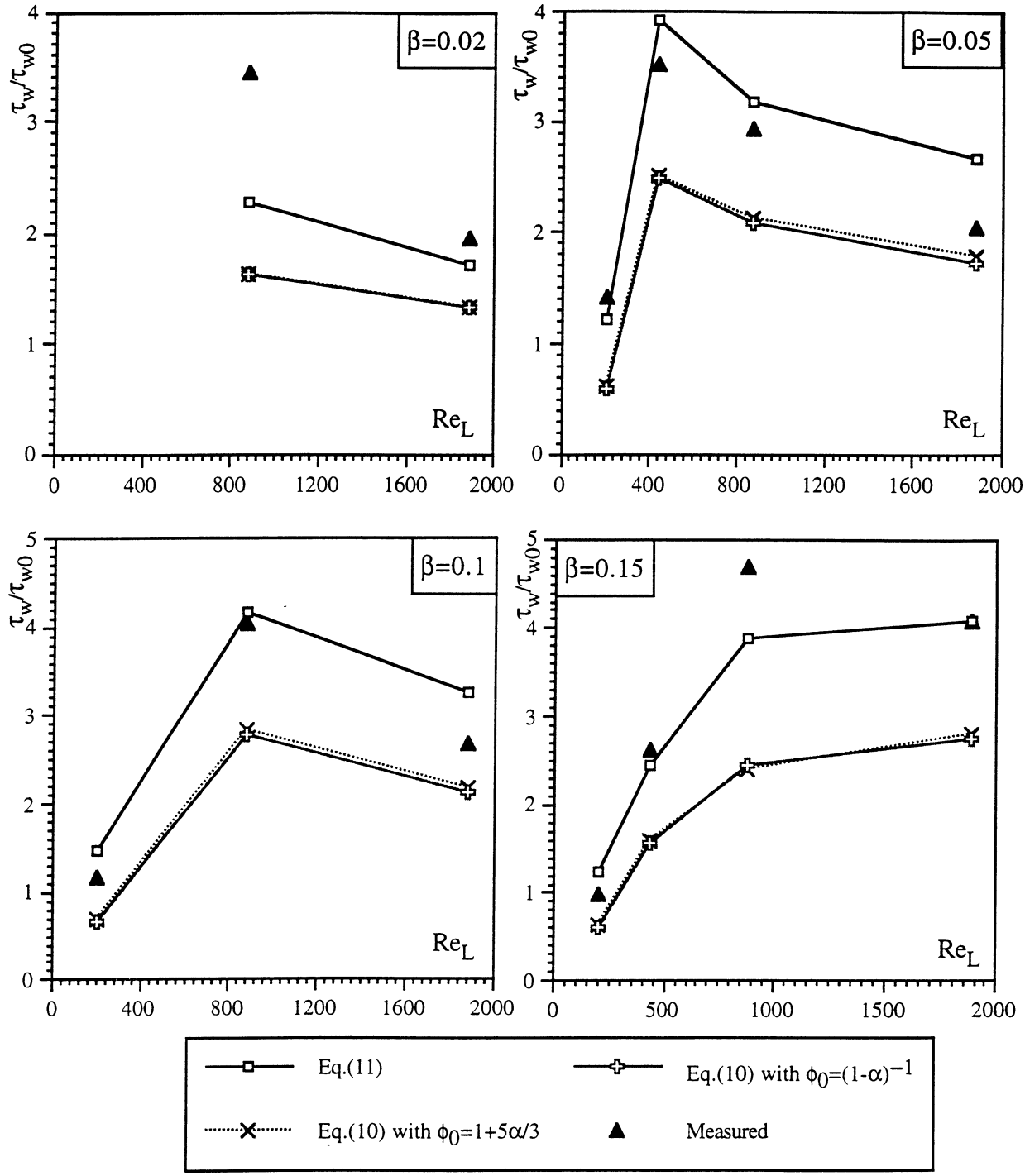

Figure 17. Comparison of predicted and measured values of τ_w/τ_{w0} (M-injector, $\nu_L = 3.5 \times 10^{-6}$ m^2/s).

Table III. Flow conditions, idealised void profile, and experimental and measured wall friction ratio in void coring regimes.

P-injector	Re_L	P	δ_1^*	α_3 (%)	δ_2^*	α_2 (%)	δ^* peak	α peak (%)	τ_w/τ_{w0} exp.	Eq. (11)	Eq. (10)
$\beta = 0.02$	106	3.30E−04	0.270	1.8	1	0.43	0.730	0.2	0.96	−1.79	0.90
	300	9.34E−04	0.068	1	0.243	0.5	0.243	1	1.10	0.91	0.95
	562	1.75E−03	0.101	5.05	1	1.56	0.676	1.3	1.09	1.43	0.95
	980	3.05E−03	0.135	7.2	1	1.85	0.676	1	1.09	1.48	0.96
$\beta = 0.1$	20	6.23E−05	0.169	2.1	0.676	1.05	0.676	2.1	−2.01	−10.59	−0.79
	980	3.05E−03	0.061	12.7	0.811	7.91	0.676	13.54	1.33	0.25	0.99
$\beta = 0.2$	11.4	3.55E−05	0.135	2.5	0.589	1.25	0.589	2.5	−7.2	−14.92	−2.6

M-injector	Re_L	P	δ_1^*	α_3 (%)	δ_2^*	α_2 (%)	δ^* peak	α peak (%)	τ_w/τ_{w0} exp.	Eq. (11)	Eq. (10)
$\beta = 0.02$	980	3.05E−03	0.041	1.31	0.171	1.02	0.124	1.58	1.00	0.99	1.00
$\beta = 0.1$	980	3.05E−03	0.030	9.45	0.634	6.55	0.507	11.1	1.33	0.69	1.05

from Timkin [13]. The comparison of experimental and predicted wall shear stress values is shown in *figure 17*: the ratio of experimental and calculated wall shear stress evolves between 1.2 and 2. These discrepancies are stronger than those observed at $\nu_L = 10 \times 10^{-6}$ m^2/s. A possible explanation is an increase of the flow asymmetry when decreasing the viscosity. Indeed, although angular distributions of wall shear stress are not available for $\nu_L = 3.5 \times 10^{-6}$ m^2/s, a very strong asymmetry was observed on the angular distributions of wall shear stress for similar conditions in water (Kashinsky et al. [14]). The ratio between the maximum and minimum values of the wall shear stress along a duct perimeter reaches 3.5 for $Re_L = 1000$ and $\beta = 24\%$. This is drastically different from the behaviour observed with a viscosity ten times higher (see *figures 11* to *13*), where the maximum deviation is about 5% with the same Re_L. Hence, although data are lacking to reach definite conclusions, the asymmetry of the flow seems to be responsible for the observed discrepancy at $\nu_L = 3.5 \times 10^{-6}$ m^2/s.

4.2. Void coring regimes

Some experimental void profiles obtained at $\nu_L = 10 \times 10^{-6}$ m^2/s exhibit a shape quite different from the one initially considered in the model (*figures 2* to *7*). First, the void peak diffuses at high Re_L. Second, void coring appears at small β for the P-injector. We tried nevertheless to fit a step function on such void distributions according to the first procedure described in *figure 14*. The parameters deduced from the experimental profiles are given in *table III*, with the experimental and calculated ratios of the wall shear stress. The incorrect predictions from equations (11) can obviously be explained by the no longer negligible relative thickness of the layers, with δ_2^* reaching 1 for the coring. On the other hand, the agreement between experimental ratios and the results predicted from equation (10) is not so bad. The discrepancy is at most 26% for negative wall shear stress. Moreover, positive values can still be predicted. Again, the moderate quantitative agreement with experiments should rely on the strong asymmetries of the angular wall shear stress distribution at these small Re_L. Thus, predictions from the complete equations (10) appear less dependent on the shape of the void profile, than those from the simplified formula (11). Their predictions seem to be reliable enough to roughly relate the influence on the liquid velocities of void fraction distributions with very different shapes.

5. Conclusions

A simple analytical model has been developed to predict the wall shear stress in laminar upward bubbly flows in circular pipes. This model relies on a three layers step-function fit of the experimental void profiles, which are thus required for any prediction. To check its validity, experiments have been performed on upward bubbly flow in a pipe in which the liquid Reynolds number was kept subcritical to avoid the inherent liquid turbulence. Void profiles and wall shear stress were measured at different flow parameters and for two gas injectors producing bubbles of different size. The void fraction radial distribution was shown to exhibit either wall peaking, or coring or even both effects. Besides, the behaviour of the wall shear agrees with previous observations: it can be either positive when downward flows occur, and for upflows, it can be as high as three times its equivalent in single-phase flow at the same liquid flow rate. Multiple wall shear stress measurements around a duct perimeter have allowed to detect strong asymmetries at low liquid Reynolds numbers.

To exploit the model, two fairly objective procedures have been proposed to fit the void profile by a step-function. Once introduced in the equation established for thick layers, they give almost similar values of the wall friction. These predictions are in good agreement with the measurements whenever the flow symmetry is ascertained. The best results are obtained in the cases where the void profiles exhibit a well-pronounced void peak close to the wall. In coring regime, implying larger bubbles ($\varepsilon > 0.10$), the agreement was less significant. Thus, the model, although only based on the action of the viscous stresses and on differential buoyancy, captures the main aspects of the liquid velocity field modifications induced by the presence of the gas. In order to improve the proposed model, a step function defined on multiple layers could be introduced to approximate the actual void profiles: in that case, the model can be also refined by taking into account the evolution of the drag force with the distance to walls.

Acknowledgements

The authors are grateful to the Russian Academy of Science and to the CNRS for support of this research under the international cooperation project n° 4089. This work was also supported by INTAS under project 96-2319.

Appendix

The factors N and D in equation (6) become:

$$N = \left(-\frac{16\phi_0^{(3)}}{R^4(1-\alpha_3)}\right)\left[A_1 + \frac{A_2}{\phi_0^{(2)}} + \frac{A_3}{\phi_0^{(3)}}\right],$$

$$D = \left(-\frac{16\phi_0^{(3)}}{R^4}\right)\left[A_1 + \frac{A_2}{\phi_0^{(2)}(1-\alpha_2)} + \frac{A_3}{\phi_0^{(3)}(1-\alpha_3)}\right],$$

$$A_1 = \frac{1}{4}\Delta_1^2\left[\Delta_2^2(\alpha_3-\alpha_2) - \Delta_1^2\alpha_2\right]\ln\left(\frac{\Delta_1}{R}\right) - \frac{1}{16}\Delta_1^4(1+2\alpha_2)$$
$$+ \frac{1}{8}(\alpha_2-\alpha_3)\Delta_1^2\Delta_2^2 + \frac{1}{8}R^2\Delta_2^2(\alpha_3-\alpha_2) + \frac{1}{8}R^2\Delta_1^2(1+\alpha_2),$$

$$A_2 = \frac{1}{4}\phi_0^{(2)}(1-\alpha_2)\left[-\alpha_2\Delta_1^4 + \Delta_1^2\Delta_2^2(2\alpha_2-\alpha_3) + \Delta_2^4(2-\alpha_2-\alpha_3)\right]\ln\left(\frac{\Delta_1}{R}\right)$$
$$+\frac{1}{4}(\alpha_2-\alpha_3)\Delta_2^4\ln\left(\frac{\Delta_1}{\Delta_2}\right) + \frac{1}{8}R^2(\Delta_2^2-\Delta_1^2)(1-\alpha_2)\phi_0^{(2)} + \frac{1}{8}\Delta_1^2\Delta_2^2\left(1-2\alpha_2+\alpha_3+(1-\alpha_2)\phi_0^{(2)}\right)$$
$$-\frac{1}{16}(1-\alpha_2)\Delta_1^4\left(1+2\phi_0^{(2)}\right) + \frac{1}{16}(1-\alpha_2)\Delta_2^4(\alpha_2+2\alpha_3-1),$$
$$A_3 = \frac{1}{4}\Delta_2^2\phi_0^{(3)}(1-\alpha_3)\left[-\alpha_2\Delta_1^2 + \Delta_2^2(\alpha_2-\alpha_3)\right]\frac{\phi_0^{(3)}(1-\alpha_3)}{\phi_0^{(2)}(1-\alpha_2)}\ln\left(\frac{\Delta_1}{R}\right) - \frac{1}{4}(\alpha_2-\alpha_3)\Delta_2^4\ln\left(\frac{\Delta_1}{\Delta_2}\right)$$
$$-\frac{1}{8}\phi_0^{(3)}(1-\alpha_3)\Delta_2^2\left[\left(1-\frac{1}{\phi_0^{(2)}}\right)\Delta_1^2 + \left(\frac{1}{2\phi_0^{(3)}}-\frac{1}{\phi_0^{(2)}}\right)\Delta_2^2 + R^2\right].$$

References

[1] Rivière N., Cartellier A., Wall shear stress and void fraction in Poiseuille bubbly flows: Part I. Analytical Predictions, Eur. J. B/Fluids (1998) (referred to as part I).

[2] Kashinsky O., Timkin L., Cartellier A., Experimental study of "laminar" bubbly flows in a vertical pipe, Exp. in Fluids 14 (1993) 308–314.

[3] Clift R., Grace J., Weber M., Bubbles, Drops and Particles, Academic Press, 1978.

[4] Kashinsky O., Randin V.V., Downward bubbly flow in a vertical pipe, Int. J. Multiphase Flow (1999), to be published.

[5] Nakoryakov V., Kashinsky O., Kozmenko B., Electrochemical method for measuring turbulent characteristics of gas-liquid flows, in: Delhaye J.-M., Cognet G. (Eds), Measuring Techniques in Gas-Liquid Two-Phase Flows, Springer, 1984, pp. 695–721.

[6] Nakoryakov V., Burdukov A., Kashinsky O., Geshev P., Electrodiffusional method for studying local structure of turbulent flows, Institute of Thermophysics, Novosibirsk, 1986.

[7] Cartellier A., Rivière N., Timkin L., New structures of Poiseuille bubbly flows due to clustering, in: Proc. ASME FEDSM'97, Vancouver, June 22–26, 1997.

[8] Kashinsky O., Timkin L., Cartellier A., Wall shear stress and velocity fluctuations in upward laminar bubbly flows, in: Celata G., Shah R. (Eds), Two-Phase Flow Modelling and Experimentation, Publ. Edizioni ETS, 1995, pp. 467–472.

[9] Cartellier A., Moechti Triyogi Y., Achard J.L., Plane Poiseuille bubbly flows: Void fraction and wall shear stress, in: Kelleher M.D. et al. (Eds), Experimental Heat Transfer, Fluid Mechanics and Thermodynamics, Vol. 2, Elsevier Science Publishers, 1993, pp. 1402–1409.

[10] Kashinsky O., Timkin L., Development of pseudo-turbulent structure in upward bubbly flows, in: Giot M., Mayinger F., Celata G.P. (Eds), Experimental Heat Transfer, Fluid Mechanics and Thermodynamics, Publ. Edizioni ETS, 1997, pp. 995–1001.

[11] Ryskin G., The extensional viscosity of a dilute suspension of spherical particles at intermediate micro scale Reynolds numbers, J. Fluid Mech. 99 (3) (1980) 513–529 (with an appendix by Ryskin G. and Rallisson J.).

[12] Kashinsky O., Timkin L., Slip velocity measurements in upward bubbly flow by combined LDA and electrodiffusional technique, in: Modern Techniques and Measurements, Proc. 2nd Int. Conf. Fluid Dynamics Measurements and Its Applications, Beijing, China, October 19–22, 1994, pp. 61–66.

[13] Timkin L., Private communication, 1997.

[14] Kashinsky O., Gorelik R.S., Randin V.V., Upward bubbly flow in a small diameter vertical pipe, Russ. J. Eng. Thermophys. 5 (1995) 177–187.